Experimental and theoretical characterization of the long-range interaction between He*(3*s*) and He(1*s*)

Nelly Bonifaci,[1,*] Frederic Aitken,[1] Vladimir M. Atrazhev,[2,†] Steven L. Fiedler,[3,‡] and Jussi Eloranta[3,§]

[1]*G2Elab-CNRS, Joseph Fourier University, 25 rue des Martyrs, 38042 Grenoble, France*

[2]*Joint Institute for High Temperatures RAS, Izhorskaya St. 13, 2 Moscow, Russia*

[3]*Department of Chemistry and Biochemistry, California State University at Northridge, 18111 Nordhoff St., Northridge, California 91330, USA*

(Received 9 November 2011; published 6 April 2012)

The long-range interaction between $^{\{1,3\}}S$ He*(3*s*) and ^{1}S He(1*s*) was studied in bulk liquid helium by fluorescence measurements and by combined theoretical electronic structure and bosonic density functional theory calculations. The excited He* atoms were produced in the liquid by corona discharge with subsequent impact excitation instigated by hot electrons from the discharge. The long-range contribution to the repulsive "hump" near 5 Å in the $^{\{1,3\}}S$ He–^{1}S He potentials was interrogated by monitoring He* $^{\{1,3\}}S(3s) \rightarrow {}^{\{1,3\}}P(2p)$ fluorescence profile characteristics as a function of external pressure between 0.1 and 3.5 MPa. Fluorescence line shifts and widths as a function of pressure were extracted from the experimental data and compared to the theoretical predictions, establishing that the nascent He* atoms reside in a bubble state within the liquid. It was observed that the experimental data could only be consistently reproduced if the excited He* atoms emit in a less-dense environment as compared with the rest of the bulk liquid.

DOI: 10.1103/PhysRevA.85.042706 PACS number(s): 34.20.−b, 78.60.Fi, 79.20.Kz, 79.70.+q

I. INTRODUCTION

Long-range forces, such as van der Waals attraction and Pauli exclusion repulsion, play an important role in both static and dynamic properties of nonchemically bound systems. Typically, such interactions lead to a pair interaction potential between two atoms that can be described by an exponential-like repulsive wall followed by an attractive interaction dictated by the dispersion coefficients. For chemically bound systems, the repulsive interaction is partially compensated by chemical bonding, which results in a much deeper minimum in the pair potential at short range. In both cases, the pair potentials have only one minimum energy distance, which determines the chemical structures of the molecules and physical characteristics of liquids and solids. Exceptions to this behavior include some molecular Rydberg systems [1–3] and molecules that possess long-range repulsive electrostatic interactions [4,5]. Such pair potentials exhibit two distinct minima, one in the molecular regime and the other near the separated atomic limit. For example, it has been suggested that it is possible to prepare a lattice of isolated atoms outside the chemically bound regime at low temperatures [6]. The interaction between excited He* and ground-state helium atoms provides another example of this type of behavior where chemical bonding occurs at short range (the bond order for Rydberg state He_2^* is one in the ground state), but the transition between the atomic and molecular Rydberg states may produce a repulsive barrier in the intermediate-distance regime.

Spectroscopic studies of intrinsic excitations (e.g., He* and He_2^*) in bulk liquid helium have a long history [7–12]. Experimental techniques, such as high-energy electron bombardment [7–9], α-particle bombardment [13,14], corona discharge [10,11,15–17], strong-field ionization by femtosecond laser pulses [18,19], vacuum ultraviolet excitation (VUV) [12], and synchrotron radiation [20–22] have been employed. The latter technique has also been applied to study intrinsic excitations and their relaxation dynamics in liquid helium droplets [23,24]. All these methods, with the exception of VUV excitation, involve the direct ionization of helium atoms as the first step, generating the corresponding positive ions and electrons in the liquid. This can directly lead to the formation of positive He_2^+ and subsequently He_2^* through electron-ion recombination, or electronically excited helium atoms He* through electron-impact ionization or excitation in the liquid. These species are formed both in their singlet and triplet electronic manifolds and they relax toward lower-energy states by emitting photons in the visible and infrared regions as well as in the VUV when the system returns to its electronic singlet ground state. The ground triplet states of He* and He_2^* are metastable because their electric dipole transitions to the ground singlet state are forbidden. In liquid helium, both the He* and He_2^* species have been established to reside inside voids with radii ranging from 7 to 15 Å ("bubble states"), which are slightly smaller than that of a solvated electron (18.5 Å radius) [25–30]. Such structures are the result of a repulsive Pauli exchange interaction between the Rydberg electron and the surrounding closed-shell helium atoms. Since the bubble radius depends strongly on the electronic state in question, both absorption and fluorescence spectra exhibit shifting and broadening due to the coupling between the Rydberg electron and the surrounding liquid ("bath"). In general, absorption lines experience stronger coupling to the surrounding bath whereas in most cases, the fluorescence lines are located closer to their gas-phase values. This behavior can be rationalized by the fact that the higher Rydberg states have a larger electron extent and thus the upper state is strongly coupled to the liquid in an absorption process whereas such coupling is

*nelly.bonifaci@grenoble.cnrs.fr
†atrazhev@yandex.ru
‡sfiedler@csun.edu
§jussi.eloranta@csun.edu

usually very small in fluorescence. However, fluorescence spectroscopy, as demonstrated in this work, can provide detailed information about repulsive upper states when the spectra are recorded systematically as a function of external pressure. Since the surrounding helium density is greater in the liquid phase as compared to helium gas, the liquid phase experiments provide better sensitivity to this interaction. There is a distinct difference between the condensed-phase and gas-phase fluorescence-line-shape behavior as a function of pressure.

Theoretical treatment of bubble states around atoms or molecules ("impurities") in liquid helium have been mostly based on the application of the well-known bubble model where the liquid part is described by the surface tension energy penalty for creating a void in the liquid ($4\pi R_b^2\gamma$; γ is the liquid surface tension and R_b is the bubble radius) with the external pressure contribution on the bubble interface included through the classical pressure-volume energy term ($P_{\rm ext}4\pi R_b^3/3$; $P_{\rm ext}$ is the external pressure) [30–33]. There are, however, several shortcomings to this approach: (1) It is not clear if there should be geometrical corrections included for the surface tension term (i.e., the Tolman correction, see Ref. [34]) and if it can be applied for nonspherical systems or for impurities with bound potentials. (2) The exact role of the often included surface kinetic energy term, which is an integral over $(\nabla\rho)^2/(8m\rho)$, is not clear and may be partially double counted as it should also contribute to the surface tension term (for discussion, see Ref. [26]). (3) The model has a poor description of the gas-liquid interface at the impurity, where the liquid density is usually described by the Heaviside step function. To provide a better microscopic description of the liquid-gas interface, a fixed trial function has often been employed (see Refs. [30–33]) but this does not exhibit the correct physical behavior in the vicinity of the impurity (e.g., a nondifferentiable abrupt behavior at the onset of nonzero liquid density). An accurate description of the liquid density in this region is very important because the calculated spectral line shapes are particularly sensitive to the liquid density profile near the impurity. While the bubble model itself does not consider the liquid-impurity interaction directly, this interaction must be present to balance the surface tension and the external pressure. This is often included in the calculation through a low-level electronic structure calculation for the impurity combined with the application of the electron-helium pseudopotential (PS) for evaluating the impurity-helium interaction PS [30,33,35]. It is difficult to judge the accuracy of such PS-based models, especially when they are used in conjunction with the semiempirical bubble model. Finally, when the bubble model has been applied to study experimental line profiles, the model parameters (e.g., surface tension) are often adjusted to match the experiment. Clearly, there is a need for a first-principles-theory model that can reproduce the spectral line shapes without empirical adjustment of any model parameters.

The most accurate theoretical methods for describing liquid helium, such as the quantum Monte Carlo approaches, are not generally applicable to systems with a large number of nuclei such as the bulk liquid [36]. Bosonic density functional theory (DFT), on the other hand, has been shown to be a computationally tractable approach capable of accurately describing solvation of impurities in liquid helium [37–41]. It can provide a more rigorous microscopic description of the liquid, especially in the gas-interface region surrounding the impurities, which is important for analyzing the spectral shifting and broadening of absorption and emission lines. Liquid helium DFT model constants are fixed against the known bulk properties and as such it does not contain any adjustable parameters [41]. While the first liquid helium DFT models were restricted to 0 K, the theory has since been extended to describe liquid helium even above the λ point [42]. The main drawback of DFT for evaluating linear optical spectra of impurities in liquid helium arises from the fact that the true many-body wave function for the liquid, which is required to evaluate the exact time-correlation function for the line shapes, is not known. Approximate methods have been developed to overcome this restriction in situations where a distinct zero phonon line and the associated phonon band appears in the spectrum [37]. In such case the frequency-domain phonon band contains information about the microscopic bath trajectory during the excitation [37,43]. However, in the present case, such structure is not present in the spectra and a simple statistical form for the time-correlation function can be applied [30,44], which does not require explicit evaluation of the liquid bath dynamics.

In this work, we have carried out spectroscopic experiments and first-principles theoretical calculations to characterize the long-range repulsive potential between $^{\{1,3\}}S$ He($3s$) and the ground-state helium atom. It is demonstrated that the current experimental approach offers a great advantage over the gas-phase measurements by yielding enhanced sampling of the pair potential and thus providing a greater sensitivity for its energetics and curvature. Bosonic DFT simulations and spectroscopic line shape calculations for singlet- and triplet-state He*($3s$) in liquid helium were carried out to model the experimental observations as a function of external pressure.

II. EXPERIMENT

A helium cryostat with an accessible temperature range between 4.2 and 300 K was employed in the experiments. To control the pressure, a copper beryllium cell, which can withstand pressures up to 11 MPa, was installed at the cold tip of the cryostat and the pressure inside the cell was measured by a capacitance manometer (MKS Instruments Micro Baratron model 890B-33PCB2GK) and the temperature by a germanium sensor (LakeShore GR-200A-2500; accuracy $\pm$0.5 mK at 4.2 K). The cell was evacuated using a turbo molecular pump (Varian 969-9351) to 10^{-6} Torr and filled with ultrapure helium (grade N 60, Air Liquide; <0.1 ppm of O_2 content). The gas was passed through a series of liquid-N_2-cooled traps filled with a mixture of molecular sieves (3 to 10 Å) and activated charcoal (prepared under vacuum at 350 °C for 3 days). The copper beryllium cell contained a discharge apparatus that was arranged in a point-plane geometry with 8 mm gap between the electrodes. The point electrode was constructed from an electrolytically etched tungsten wire (1 mm diameter). The present experiments employed 0.45 μm and 2.5 μm point electrodes for positive and negative polarities, respectively, as determined by electron

microscopy (Jeol JSM 5600LV). The plane electrode was constructed from copper (20 mm diameter). The voltage to the electrodes was supplied by a stabilized dc power supply (Spellman model RHSR/20PN60) giving either positive or negative tip polarity. The current was monitored by a Keithley 610 C ampere meter. Discharge current and power in the liquid phase (4.2 K) were in the range of 0.1 to 0.5 μA and 0.5 to 3.0 mW and in the gas phase (300 K) 20 to 50 μA and 20 to 100 mW. The observed corona discharge threshold voltages were observed to be independent of pressure.

Both the helium cryostat and the copper beryllium cell were equipped with sapphire windows, which allowed the collection of light near the corona discharge zone by a short focal length lens. A second quartz lens was used to focus the light into a 300-mm-focal-length spectrograph (Acton Research Corporation; Spectra-Pro-300i with 150 groves/mm and 1200/groove/mm gratings). A liquid-N_2-cooled charge coupled device (CCD; Princeton Instruments model 2D-CCDTKB-UV/AR) was installed at the exit plane of the spectrograph. The spectral resolution with the 1200 groove/mm grating was 0.1 nm as determined from the spectral profiles of argon discharge lamp lines. The two relevant atomic He* lines observed in the experiments through fluorescence are the triplet He* line at ca. 706 nm [^3S He($3s$) $\rightarrow$ ^3P He($2p$)] and the singlet He* line at ca. 728 nm [^1S He($3s$) $\rightarrow$ ^1P He($2p$)].

III. THEORY

The $^{\{1,3\}}S$ He*($3s$)–^1S He($1s$) and $^{\{1,3\}}P$ He*($2p$)–^1S He($1s$) pair interactions were obtained by using the full configuration interaction (CI) method as implemented in the MOLPRO code [45,46]. The full CI method is a size-consistent approach, which allows us to correct for the basis set superposition error (BSSE) through the approach of Boys and Bernardi [47]. Provided that the basis set convergence is sufficient, this approach has been shown to provide highly accurate results for rare-gas systems even with a limited treatment of electron correlation (typical accuracy ca. 1 cm^{-1}) [48,49]. The calculations in this work employed the basis set given by Refs. [50,51] ("basis 1"). A test for basis set convergence was carried out by comparing the results against a larger basis set developed by Deguilhem ("basis 2"; basis set "E" as specified in appendix A of Ref. [52]). Both basis sets provide the correct description of the relevant atomic asymptotes up to the $3p$ level.

The liquid helium surrounding He* was modeled by bosonic DFT where the He*-He pair potential obtained above acted as an external potential for the liquid. An extension of the DFT model of Stringari *et al*. (the Orsay-Trento functional) was used to model the liquid when $T > 0$ K [41,42]. At present, the calibration of the model has been performed up to 3 K and we have used this temperature to mimic the 4.2 K experimental conditions. This approximation will result in a slight underestimation of the ideal gas contribution to the functional, which is particularly important in the low-pressure regime. Due to the reduced liquid-gas interface width, this approximation will result in a small underestimation of the fluorescence line blueshift. The external pressure was accounted for by adjusting the bulk liquid density according to the known equation of state for liquid helium at the given temperature [53]. In addition to the bosonic DFT description for the liquid degrees of freedom, the zero-point motion for He* was included in the model by minimizing its energy simultaneously with the liquid DFT equation. The interaction energy functional between the two systems is given by

$$E[\psi_{\mathrm{He}^*},\psi_{\mathrm{liq}}] = \int\int |\psi_{\mathrm{He}^*}(r)|^2 V_{\mathrm{He}^*\text{-He}}(|r-r'|)|\psi_{\mathrm{liq}}(r')|^2 d^3r' d^3r, \quad (1)$$

where ψ_{He^*} is the He* wave function localized inside the bubble, ψ_{liq} is the liquid helium order parameter, and $V_{\mathrm{He}^*\text{-He}}$ represents the He*-He pair potential. The appropriate functional derivatives of Eq. (1) were included in the imaginary-time propagation procedure for solving the resulting coupled nonlinear Schrödinger-type equations (i.e., He* nuclear motion and liquid DFT) [54]. The numerical treatment of the helium DFT problem is described elsewhere [55]. To minimize the boundary condition artifacts arising from using a finite simulation box, a large grid consisting of $256 \times 256 \times 256$ points with a spatial grid step of 1.0 bohr was used in the calculations. An imaginary time step length of 80 fs was used in minimizing the total energy of the system. To verify that time-step bias was not present, shorter times steps down to 10 fs were executed at the end of each run. Typically 150 imaginary time iterations were required for full convergence. The resulting liquid density profiles were subsequently employed in evaluating the spectral line shapes (see below). The coupled He*-He DFT solver was implemented in parallel by using the published LIBDFT [56] and LIBGRID [57] libraries.

The experimentally observed fluorescence line shapes do not show any distinct zero phonon and phonon wing structure, which indicates that the associated time correlation function decays faster than any dynamic mode of the liquid. It has been shown previously that several liquid modes may give additional structure to absorption or emission lines: bubble breathing motion as well as maxon- and roton-region excitations in the bulk dispersion relation [37]. Since the current experiments were carried out well above the λ transition, the stationary liquid excitations (i.e., rotons and maxons) experience strong lifetime broadening such that they cannot be spectrally resolved. The bubble breathing mode is not expected to yield discrete structure since this mode is strongly overdamped with the current pair potentials. Consequently, in the present case it is possible to use Anderson-type static formulation for the time correlation function, $c(t)$ [26,44]:

$$c(t) = \exp\left\{ -\iint \left[1 - \exp\left(-\frac{i\Delta V(|R-r|)t}{\hbar} \right) \right] \times \rho_{\mathrm{He}^*}(R)\rho_{\mathrm{liq}}(r) d^3R d^3r \right\}, \quad (2)$$

where ΔV is the difference pair potential between the excited and ground states corresponding to the emission line, $\rho_{\mathrm{He}^*} = |\psi_{\mathrm{He}^*}|^2$ and $\rho_{\mathrm{liq}} = |\psi_{\mathrm{liq}}|^2$. Note that this expression incorporates the zero-point motion for He* into the evaluation of the time-correlation function. It has been shown previously that the interfacial dynamics is the fastest mode in the bubble dynamics, which typically proceeds on a timescale less than 10 ps [25]. In the present case, the time scale of the dynamics occurring on the lower $2p$ state was estimated to be 3 ps by

propagating the $3s$ equilibrium density subject to the He*$(2p)$-He potential in real time and by observing the penetration of the liquid into the nodal plane of the occupied $2p$ orbital. This mode is slower than the time-correlation function decay time extracted from the observed experimental fluorescence linewidth. Based on this estimate, Eq. (2) provides an accurate description of the fluorescence line shape. Fourier transform of $c(T)$ will then yield the frequency-domain spectrum, which allows for direct comparison between the experimental data and the theoretical calculations.

IV. RESULTS AND DISCUSSION

Corona discharge in a point-plane geometry has been used to ionize helium and study charge transport phenomena in liquid helium over a wide range of hydrostatic pressures. Close to the point electrode, the onset of the ionization process essentially determines the voltage threshold for corona discharge (ca. 3 to 4 kV). The strong electric field near the point electrode initiates an electron avalanche proceeding through a series of electron-helium impact events, causing an exponential increase in the charge density that leads to a distortion of the electric field (i.e., non-Laplacian field). Effectively this process creates a small highly ionized volume ($<10\ \mu m^3$) near the tip. The ions that escape the ionization volume are subject to the reduced electric field that is present in the interelectrode space ("drift zone"). The interaction of ions (i.e., electrons in negative corona and He^+ in positive corona) with the liquid determines their mobility and thus the observed corona current. The mobilities of the ions are affected by their primary microscopic solvation structures ("bubble" for electrons and "snowball" for positive ion) as well as by the external pressure, which perturbs the solvation structures. If the density of the charges in the drift zone is such that the ions interact, the corona current exhibits a quadratic dependency on the applied voltage. In liquid helium, the observed corona current is limited to less than 0.5 μA due to the rather low ion mobility in the liquid.

It is important to first identify the spatial origin of the observed He* emission lines (i.e., bulk liquid or dense gas). The discharge zone is expected to be at a higher temperature than the rest of the liquid because the electron or ion current power density is unevenly distributed between the electrodes and the discharge zone is thermally insulated from the rest of the liquid due to the momentum mismatch between the gas and the liquid. Note that even below the λ point, the latter would occur through the well-known Kapitsa resistance effect [58]. If the height of the long-range repulsive hump in the He*-He potential (approximately 120 cm^{-1} at 5 Å for the triplet state He*) is smaller than the thermal energy kT available, the system would instead emit from the lower-energy molecular states. The long-range repulsive hump can be thought to act as a filter for producing either the molecular excimer or atomic He*. Thus the present set of experiments detect atomic He* fluorescence lines, which most likely originate from outside the discharge region. Direct experimental evidence for He* emitting in the bulk liquid can be obtained by comparing the pressure dependency of the emission line shift for gas vs liquid (see Fig. 1). Due to the low density in the gas phase, the line shift is very small but the spectral broadening is significant due

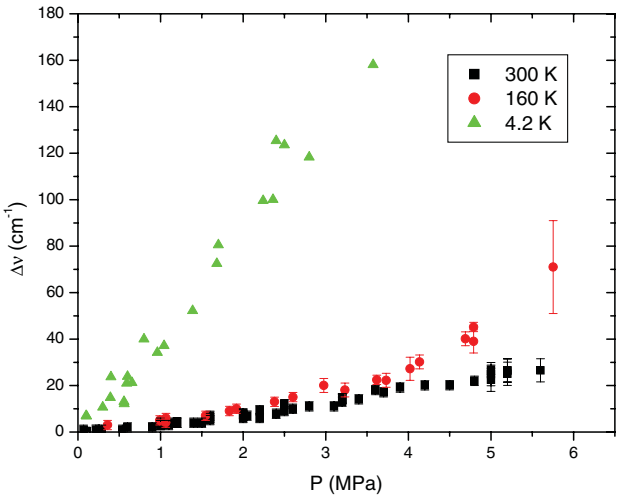

FIG. 1. (Color online) Shift of the ^3S He* 706 nm fluorescence line ($\Delta\nu$) in gas (300 K and 160 K) and liquid (4.2 K) phases. Note that the blueshift in the liquid phase depends strongly on the pressure.

to frequent random collisions with gas-phase He atoms. Conversely, in the liquid, the higher helium density around He* results in both a large blueshift as well as line broadening. Both the observed singlet and triplet He* lines exhibit similar pressure-dependent behavior (apart from quenching) indicating that both species reside in the bulk liquid solvated in bubble states.

To assess the effect of increased external pressure (P) in sampling the repulsive wall of the long-range hump ($V_{\text{He*-He}}$; $R > 5$ Å), it is instructive to write the fluorescence line shift (represented by ΔE) in terms of reduced liquid density ρ/ρ_0:

$$\Delta E = \int \rho(r) V_{\text{He*-He}}(r) d^3r = \frac{P}{kTZ} \int \frac{\rho(r)}{\rho_0} V_{\text{He*-He}}(r) d^3r, \tag{3}$$

where the bulk density $\rho_0 = P/(kTZ)$ is determined by the liquid thermodynamic equation of state (Z is the compressibility factor, k is the Boltzmann constant, T is the temperature). If the integral in Eq. (3) remains constant (i.e., independent of P or T), a plot of ΔE against P/Z should show linear behavior [or against $1/(TZ)$]. For the triplet He* emission line, this occurs at pressures $P > 1.5$ MPa. Below this limit, the value of the integral also changes as a function of pressure indicating that different parts of the repulsive potential are being sampled by the liquid. Equation (3) can also be used to rationalize the observed near-linear behavior of the line shift as a function of pressure (or inverse temperature).

The radiative lifetime of $^{\{1,3\}}$He*$(3s)$ is on the order of nanoseconds, which is too short for He* to diffuse into the surrounding liquid from the discharge region. A plausible formation mechanism for He* in the bulk liquid is through electron-impact excitation by hot electrons from the discharge zone propagating in the conduction band of the liquid (begins at ca. 1 eV above the localized bubble state):

$$e^- + \text{He} \rightarrow \text{He}^* + e^- + \text{heat}, \tag{4}$$

where the electron loses part of its kinetic energy in the collision and an excited He* is created. For example, previous high-energy electron bombardment and VUV irradiation

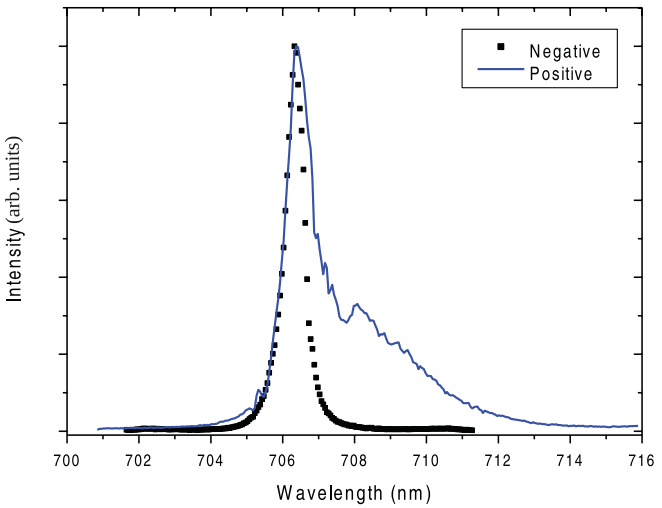

FIG. 2. (Color online) Comparison of He* $^3S\,(3s) \rightarrow {}^3P\,(2p)$ 706 nm emission line at $T = 4.2$ K and $P = 0.1$ MPa with positive and negative tip polarities.

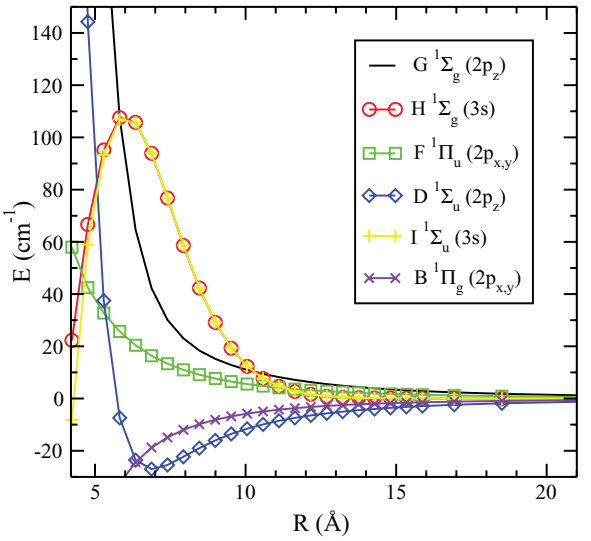

FIG. 3. (Color online) Singlet He*-He pair potentials correlating with the $3s$ and $2p$ atomic asymptotes (basis set 1). The atomic limits have been shifted to a common origin to show the details of the potentials. The state labels have been assigned based on previous spectroscopic studies [60].

experiments have shown that the nascent molecular excimer species have extremely high vibrational and rotational states populated (i.e., high molecular temperature) indicating that such processes deposit the excess energy locally into the system [20,59]. The process depicted in Eq. (4) occurs at much lower temperature (i.e., in the bulk liquid) than the discharge zone, hence stabilizing the nascent He*. Evidence for this mechanism can be obtained by reversing the tip polarity from negative to positive. In the former case the electrons are ejected from the tip by the electric field into the liquid and therefore the process described by Eq. (4) proceeds efficiently in the bulk. With positive tip polarity, the electrons are retained near the discharge zone by Coulomb attraction, which greatly reduces the efficiency of Eq. (4) in the bulk. A comparison of the He* 706 nm emission line is shown in Fig. 2 where it is clearly observed that the positive tip configuration results in a broader line as well as in the emergence of a new broad band to the red of the main line. The new band is also located slightly to the red of the gas-phase line origin and does not exhibit significant pressure dependence. Based on the lack of pressure dependence of the line position and the large linewidth, the band is likely to originate from the gaseous discharge region. Deconvoluting the experimental line profile by using two Lorentzians (i.e., the main line and the redshifted feature) gives a redshift for the band as 13 cm^{-1} and the width as 53 cm^{-1} ($P = 0.14$ MPa). However, at present the exact origin of this band is unknown as the current *ab initio* potentials can only predict a blueshift. It is possible that, when the discharge occurs in a volume confined by the liquid, the temperature and pressure may be such that they have not been explored in the earlier gas-phase studies. For example, an efficient sampling of the long-range maximum near 5 Å (see Figs. 3 and 4) may be sufficient to produce such a redshift. Note that, in this distance regime, many-body effects, which are not included in our current calculations, are also expected to play an important role. The conclusion is therefore that a negative tip polarity should be used in order to obtain better thermalized He* in the bulk liquid. As indicated in Eq. (4), the electron-impact process will also release heat to the immediate surroundings of the He* formed in the bulk liquid ("local heating"), which, as discussed below, has important implications for the appearance of the fluorescence line shape.

The calculated pair potentials for $^{\{1,3\}}S$ He($3s$)–^1S He($1s$) and $^{\{1,3\}}P$ He($2p_{\{x,y,z\}}$)–^1S He($1s$) are shown in Figs. 3 and 4. The repulsive hump around 5 Å distance corresponds to the Rydberg transition regime, going from the atomic He* to the molecular He_2* [2]. In both the singlet and triplet manifolds,

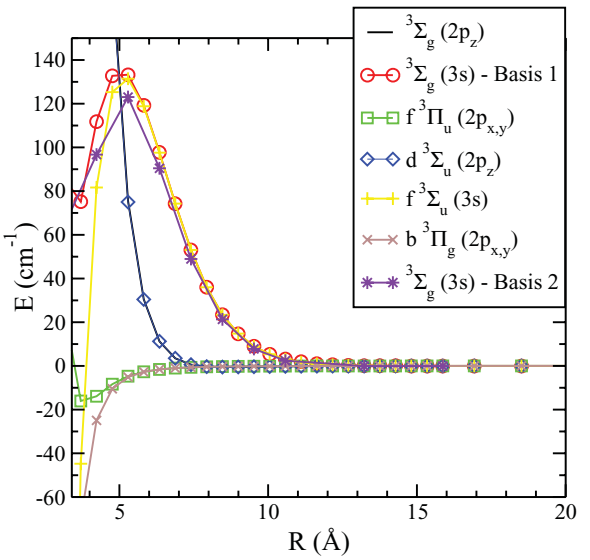

FIG. 4. (Color online) Triplet He*-He pair potentials correlating with the $3s$ and $2p$ atomic asymptotes. The atomic limits have been shifted to a common origin to show the details of the potentials. Two different basis sets ("basis 1" and "basis 2") were applied for the $3s$ $^3\Sigma_g$ states to study the basis set convergence. The state labels have been assigned based on previous spectroscopic studies [60].

TABLE I. Long-range pair potential data for ^3S ($3s$) He*–^1S ($1s$) He obtained from full CI calculations employing "basis 2."

R (Å)	E (cm^{-1})	R (Å)	E (cm^{-1})
16.0	0.0	10.0	4.6
15.5	− 0.2	9.5	8.0
15.0	− 0.3	9.0	13.1
14.5	− 0.3	8.5	20.6
14.0	− 0.2	8.0	31.2
13.5	− 0.1	7.5	45.7
13.0	0.0	7.0	64.2
12.5	0.3	6.5	84.6
12.0	0.7	6.0	105.0
11.5	1.2	5.5	121.4
11.0	1.8	5.0	119.3
10.5	2.5	4.5	104.7

there are two molecular states that originate from the $3s$ He asymptote, Σ_g and Σ_u. At distances greater than 7 Å, these molecular states remain degenerate as the system does not experience the molecular regime yet. The same applies for the $2p$ asymptote regarding the u and g molecular states whereas a small breaking of degeneracy can be seen between the Σ and Π states that arises from this asymptote. However, considering the relevant range of the experimental observations, the $2p$ potentials for the triplet state appear to be essentially flat when $R > 5$ Å as compared to the $3s$ state. Consequently, it is not necessary to consider all the possible molecular state combinations in simulating the fluorescence spectrum for the $3s$-$2p$ transition (see below). This does not hold for the singlet state and it was necessary to consider the additionally split $2p$ states based on the standard molecular selection rules. The basis set convergence for the triplet state was tested by using an extended basis set ("basis 2"; see Fig. 4; tabulated numerical data given in Table I). The application of the larger basis set lowered the height of the long-range repulsive hump near 5 Å by 12 cm^{-1}. The difference becomes gradually smaller at larger distances where both potentials are in general within a couple of cm^{-1} from each other.

The calculated liquid density profiles from bosonic DFT as a function of external pressure are summarized in Figs. 5 and 6. As the bubbles formed around He* have fairly large radii and essentially no binding in the external potential, the liquid profiles are very smooth with only weak density oscillations due to liquid correlations visible, especially at higher external pressures. The effect of external pressure on the liquid density near the He* is remarkable, allowing experiments to probe the long-range region of the repulsive hump effectively over several different distances. Thus it is clear that the experimentally observed line shifts and broadening must be very sensitive to the pair potential in this regime, although indirectly as the potential is convoluted with the liquid density. Note that, in the gas phase, the behavior is completely different, as demonstrated in Fig. 1. In the limit of high pressure, tunneling or hump crossing will eventually lead to the destruction of He* and to the formation of He_2*. Based on the experiments, the fluorescence quenching of He* occurs after $P = 0.6$ MPa for the singlet state and after $P = 3.5$ MPa for the triplet state. This is the expected trend based on the

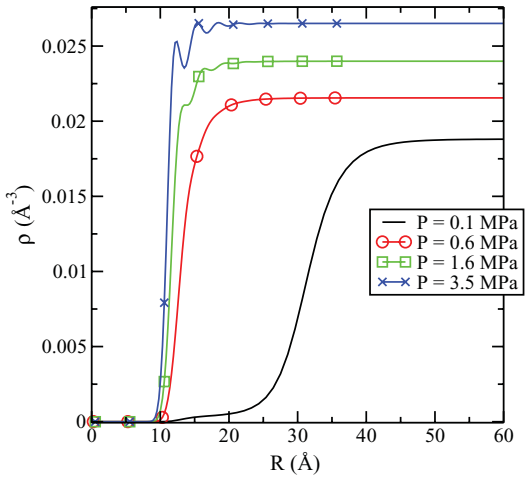

FIG. 5. (Color online) Liquid helium density profiles around singlet state He* ($3s$) at 4.2 K as a function of external pressure (employing basis 2 data). The density asymptotes have been fixed to the known densities based on the literature values [53]. The zero-point density widths (full width at half maximum; FWHM) for He* range from 0.8 Å at 3.5 MPa to 3.5 Å at 0.1 MPa.

results shown in Figs. 3 and 4 as the triplet state long-range hump height is higher than for the singlet state. However, an additional quenching mechanism for the singlet state must be present because the difference between the barrier heights (ca. 20 cm^{-1}) appears too small to fully account for such a difference.

A comparison between the experimental and theoretical line shifts as a function of external pressure is shown in Fig. 7. As the accessible pressure range for the singlet-state emission line is very small, consideration was limited to the triplet emission line, which shows no pronounced fluorescence

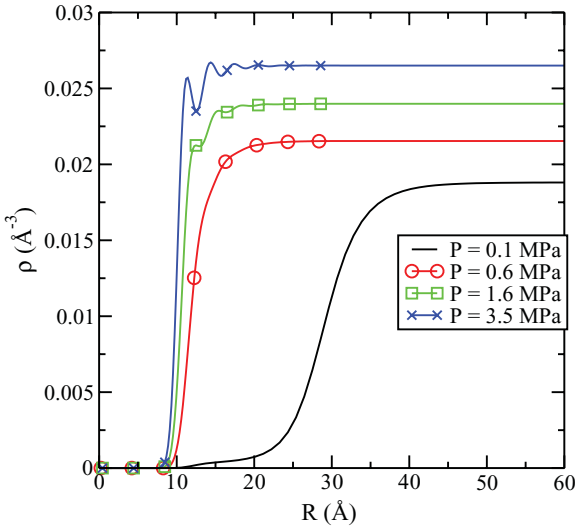

FIG. 6. (Color online) Liquid helium density profiles around triplet state He* ($3s$) at 4.2 K as a function of external pressure (employing basis 1 data). The density asymptotes have been fixed to the known densities based on the literature values [53]. The zero-point density widths (FWHM) for He* range from 0.8 Å at 3.5 MPa to 3.3 Å at 0.1 MPa.

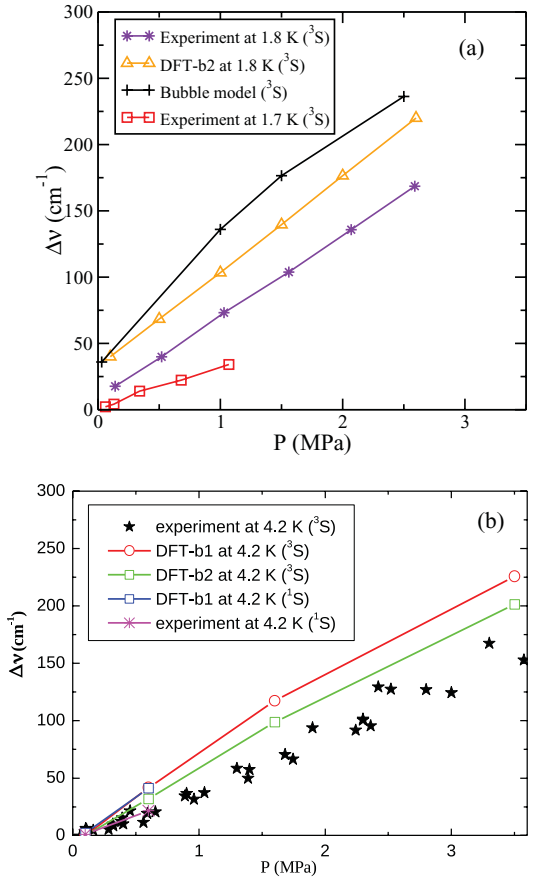

FIG. 7. (Color online) He* singlet (728 nm line) and triplet (706 nm line) fluorescence line shifts ($\Delta\nu$) as a function of external pressure. Panel (a) summarizes the data below the λ point and panel (b) at 4.2 K (this work). The 1.8 K data were taken from Ref. [8] and the 1.7 K data from Ref. [10]. DFT indicates results from the DFT calculations with the applied *ab initio* basis set indicated as "b1" or "b2" corresponding to "basis 1" or "basis 2." The line shifts were calculated using Eq. (2). ^3S in the caption denotes the He* $^3S(3s) \rightarrow {}^3P(2p)$ emission and ^1S the corresponding singlet transition.

quenching below 3.5 MPa. In general, both the PS or bubble model calculations of Lane *et al.* [30,33] and the present *ab initio* or DFT calculations produce larger blueshifts than observed experimentally (see Fig. 7). Below the λ point, the *ab initio* or DFT model produces a linear pressure dependence and a smaller blueshift as compared with the PS or bubble model. There are three possible sources for the excess blueshift predicted by the present calculations: (1) error in the He*-He pair potential, (2) reduced helium density surrounding He* as compared to the rest of the bulk liquid, or (3) an error in the experimentally determined absolute line position under the saturated vapor pressure conditions.

Regarding the first possibility, we note that both theoretical models (PS or bubble model and *ab initio* or DFT) produce the same blueshift near the saturated vapor pressure conditions at 1.8 K (see Fig. 7) and they further predict a similar trend in the increase of the blueshift as a function of pressure. The PS and *ab initio* methods used to derive the He*-He interaction potential are quite different from each other and it would be a curious coincidence that the two methods would reproduce the same saturated vapor pressure result by accident. Furthermore, a similar triplet He*-He pair potential with a lower level electron correlation treatment was applied successfully to model the gas-phase line broadening of the same transition indicating that our potential must have sufficient accuracy [61]. The *ab initio* or DFT approach has also been used previously to model the He_2^* ($^3c \leftarrow {}^3a$ transition) absorption spectrum with an accuracy of ca. 5 cm^{-1} [26]. In this case, experiments employed the cold electron emission technique (i.e., $He_2^+ + e^- \rightarrow He_2^*$ in the liquid with low excess kinetic energy available for the electron), which produced 50 cm^{-1} larger blueshift than observed with the electron beam method [9,16,59]. Note that, due to the $He^+ + He \rightarrow He_2^+$ channel, this approach is not applicable for creating He* species in liquid helium.

Considering the second possibility, a reduced liquid density around He* may be caused by an increased local temperature when excess energy is released to the surrounding liquid during the electron localization process as shown in Eq. (4). In a time-dependent picture, a plausible model for this process is as follows: (1) the excess energy rapidly heats a fixed volume of helium surrounding the He* such that it turns into gas, (2) the gaseous region ("microscopic gas bubble") begins to expand because its internal pressure is higher than the external pressure (includes the liquid surface tension) imposed by the rest of the system, and (3) expansion proceeds until both pressures are equal or the gas bubble cools down to become liquid again. Note that, at least initially, the helium density in the gas bubble remains high and He* is located in a bubble state there. If the gas bubble expansion process occurs on a comparable time scale as the fluorescence lifetime (nanoseconds), He* would experience a bath interaction that depends on a time average of the helium density during the gas bubble trajectory. This time scale depends strongly on the initial bubble radius (i.e., the volume) as well as the initial internal pressure. For example, small molecular excimer bubbles exhibit fairly rapid expansion times ca. 70 ps in superfluid helium, but the expansion rate would decelerate with increasing bubble radius, which dictates the effective mass of the moving gas-liquid interface [19]. On the other hand, larger macroscopic gas bubbles generated by laser heating are known to exist in superfluid helium on the millisecond time scale [62]. Unfortunately, since the initial internal pressure of the gas bubble is not known, it is not possible to provide a reliable estimate for its expansion time. Based on this model, the experimentally observed variations in the line shift are caused by the excess heat deposited during the He* preparation and the consequent reduction in the surrounding helium density. This introduces an artificial redshift for the experimental emission lines that depends on the amount of excess energy deposited. The difference between the experimental and theoretical line shifts in terms of pressure, as shown in Fig. 7(a), is ca. 0.5 MPa, which corresponds to a liquid density difference of 10 kg/m^3. At 1.0 MPa external pressure, this can be related to a local temperature increase from 4.2 to 5.3 K. Such an effect is expected to saturate quickly because the fluorescence signal is only sensitive to the immediate neighborhood of the emitter and the deposition of just 1 eV electron localization energy into the surroundings is sufficient to provide every helium atom within a 30 Å^3 volume 4 K of kinetic energy. In the applied power range no

changes in the fluorescence spectra were observed. Note that it is not possible to vary the parameters freely while preserving the discharge characteristics.

To rule out the third possibility, additional experiments below the λ point would have to be carried out to clarify whether the previously determined position for the 706 nm line under saturated vapor pressure is correct. An error in the line origin could easily explain the observed nearly constant offset between the experiment and theory. For example, the zero pressure line position ($\lambda = 706.0$ nm) observed in electron beam irradiation experiments may have limited accuracy due to instrumental factors (e.g., monochromator resolution, calibration). Furthermore, it appears that emphasis in these experiments was placed on the relative pressure dependency rather than on the absolute line positions [8]. On the other hand, such errors cannot explain the observed differences at 4.2 K, as we have carefully determined the line positions at sufficiently high resolution by using a calibration lamp. Furthermore, at this temperature, the low-pressure limit for the line position corresponds closely to the known gas-phase value thus providing a convenient additional source of calibration. It should be noted that, at 4.2 K, we also expect our theoretical model to slightly overestimate the blueshift due to the fact that the functional was calibrated at 3.0 K and this may partially explain the observed difference.

The extension of the basis set in the *ab initio* calculations (i.e., going from basis 1 to basis 2) produces a slightly reduced blueshift but the difference is still smaller than the overall offset between experiment and theory. To improve the accuracy of the calculations beyond what is considered here, many-body effects in the He*-He potential should also be included. However, this would be expected to produce a small additional spectral blueshift, which acts in the opposite direction as compared to the experimental results discussed above.

While the line shift is mainly sensitive to the overall energetics of the He*-He potential [cf. Eq. (3)], the linewidth is more influenced by the curvature of the $3s$ potential. The pressure dependence of the experimental and theoretical linewidths for the triplet state He* are shown in Fig. 8. At 1.8 K, similar differences are observed as in the line shift vs pressure data, and the overestimation of the linewidth by theory can also be related to the reduced helium density around He* (i.e., the increased local temperature). The local temperature difference around the He* at 4.2 K is significantly lower than at 1.8 K (based on the above line-shift analysis) and thus the 4.2 K linewidths also correspond more closely to the theoretical prediction. For the singlet-state He*, the linewidth comparison (not shown) is complicated by the fact that the experimental data can only be obtained up to 0.6 MPa due to fluorescence quenching and that multiple electronic transitions must be considered as the states correlating with the $2p$ atomic asymptote are no longer flat in the region of interest (i.e., the true difference potential must be used). To address the latter issue, it is necessary to consider multiple transitions using the molecular selection rules. However, there is still a large discrepancy between the experimental (1.38 nm) and theoretical linewidths (0.2 nm) at $P = 0.1$ MPa. This can be understood in terms of resonance broadening due to the lower $2p$ state having a strongly resonant transition down to

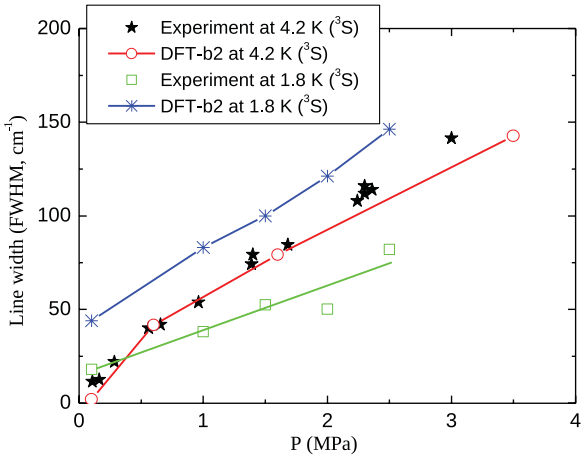

FIG. 8. (Color online) He* triplet (gas-phase 706 nm line) fluorescence linewidths (FWHM) as a function of external pressure. The 1.8 K data were taken from Ref. [8] and the 4.2 K data were obtained in this work. DFT-b2 represents the theoretical results from DFT calculations with basis 2 used in the *ab initio* calculation of the pair potential. ^3S in the caption denotes the He* $^3S(3s) \rightarrow {}^3P(2p)$ emission.

the electronic singlet ground state ($1s$). The resonance line broadening can be estimated, [63] viz

$$\Delta\lambda_{1/2}^{R} = 8.6 \times 10^{-30} \sqrt{g_i/g_k}\,\lambda^2 \lambda_r f_r N_i, \qquad (5)$$

where λ is the wavelength of the observed line (nm), f_r is the oscillator strength of the transition, λ_r is the wavelength of the resonance line (nm), g_i and g_k are the degeneracy factors of the upper and lower resonant states, correspondingly, and N_i is the number density of the atoms (dm^{-3}). This estimate yields a linewidth of 1.3 nm, which can be compared with the experimental linewidth of 1.4 nm at $P = 0.1$ MPa. The residual linewidth is therefore 0.1 nm, which is essentially the same as predicted by the theory.

V. CONCLUSIONS

We have developed an accurate pair potential for He*($3s$)-He in both singlet and triplet states using full CI calculations. The accuracy of the potentials were validated by comparison with experimental spectroscopic data where the fluorescence signal was obtained from He* embedded in liquid at 4.2 K. By analyzing the He* line shifts as a function of pressure, it was shown that He* resides inside bubbles, which in turn may be surrounded by a lower-density region created by the excess energy released during the electron-He excitation process. The degree of local heating depends on the He* preparation method as demonstrated by comparing our 4.2 K data with a similar experiment carried out at 1.8 K. Due to fluorescence quenching of the singlet He* line after 0.6 MPa, it was not possible to assess the singlet-state-potential accuracy in detail. However, a comparison of the limited experimental and theoretical data indicates that the singlet-state He* also resides in similar bubbles in the liquid as the triplet-state He*.

The experimental technique applied provides a sensitive probe for interrogating the long-range repulsive interactions as the liquid density can be varied over a wide range. This

is in contrast to gas-phase conditions where helium density is much lower and the gas therefore cannot sample the pair interaction potential as efficiently as in the liquid phase. The extended range of the liquid coverage over the He^*-He pair potential was also demonstrated by bosonic DFT calculations as a function of pressure, which clearly showed the efficient liquid density sampling of the long-range part of the repulsive hump in the pair potential. At pressures greater than 1.5 MPa, the line shifting was observed to result solely from the increase in the surrounding helium density rather than more efficient sampling of the long-range repulsive wall.

ACKNOWLEDGMENTS

Financial support from the US National Science Foundation grant CHE-0949057 to J.E. and S.L.F. and Russian Foundation of Basic Research Grant No. 09-08-01063 to V.M.A. are gratefully acknowledged. J.E. would also like to thank the Joseph Fourier University for the financial support during his stay at Grenoble. Additional computational resources were provided by the US National Science Foundation through TeraGrid resources at the National Center for Supercomputing Applications (NCSA) under Grants No. TG-CHE100150 and No. TG-CHE110056.

[1] M. L. Ginter and R. Battino, J. Chem. Phys. **52**, 4469 (1970).
[2] L. Guberman and W. A. Goddard, Phys. Rev. A **12**, 1203 (1975).
[3] D. Vrinceanu, S. Kotochigova, and H. R. Sadeghpour, Phys. Rev. A **69**, 022714 (2004).
[4] L. Bytautas and K. Ruedenberg, J. Chem. Phys. **130**, 204101 (2009).
[5] F. A. Evangelista, E. Prochnow, J. Gauss, and H. F. S. III, J. Chem. Phys. **132**, 074107 (2010).
[6] J. Eloranta, Low Temp. Phys. **162**, 718 (2011).
[7] W. S. Dennis, J. E. Durbin, W. A. Fitzsimmons, O. Heybey, and G. K. Walters, Phys. Rev. Lett. **23**, 1083 (1969).
[8] F. J. Soley and W. A. Fitzsimmons, Phys. Rev. Lett. **32**, 988 (1974).
[9] J. W. Keto, F. J. Soley, M. Stockton, and W. A. Fitzsimmons, Phys. Rev. A **10**, 872 (1974).
[10] P. H. Zimmermann, J. F. Reichert, and A. J. Dahm, Phys. Rev. B **15**, 2630 (1977).
[11] V. A. Goncharov and V. I. Levitov, Izv. Akad. Nauk, Energ. i Transport **12**, 134 (1975).
[12] C. M. Surko and F. Reif, Phys. Rev. **175**, 229 (1968).
[13] J. Jortner, L. Meyer, S. A. Rice, and E. G. Wilson, Phys. Rev. Lett. **12**, 415 (1964).
[14] F. E. Moss and H. L. Hereford, Phys. Rev. Lett. **11**, 63 (1963).
[15] S. G. Kafanov, A. Y. Parshin, and I. A. Todoshenko, JETP **91**, 991 (2000).
[16] A. Y. Parshin, I. A. Todoshenko, and S. G. Kafanov, Physica B **91**, 284 (2000).
[17] Z.-L. Li, N. Bonifaci, F. Aitken, A. Denat, K. von Haeften, V. M. Atrazhev, and V. A. Shakhatov, Eur. Phys. J. Appl. Phys. **47**, 22821 (2009).
[18] A. V. Benderskii, R. Zadoyan, N. Schwentner, and V. A. Apkarian, J. Chem. Phys. **110**, 1542 (1999).
[19] A. V. Benderskii, J. Eloranta, R. Zadoyan, and V. A. Apkarian, J. Chem. Phys. **117**, 1201 (2002).
[20] K. von Haeften, A. R. B. de Castro, M. Joppien, L. Moussavizadeh, R. von Pietrowski, and T. Moller, Phys. Rev. Lett. **78**, 4371 (1997).
[21] K. von Haeften, T. Laarmann, H. Wabnitz, and T. Moller, Phys. Rev. Lett. **88**, 233401 (2002).
[22] K. von Haeften, T. Laarmann, H. Wabnitz, and T. Moller, J. Phys. B **38**, S373 (2005).
[23] K. von Haeften, T. Laarmann, H. Wabnitz, T. Möller, and K. Fink, J. Phys. Chem. A **115**, 7316 (2011).
[24] O. Kornilov, O. Bünermann, D. J. Haxton, S. R. Leone, D. M. Neumark, and O. Gessner, J. Phys. Chem. A **115**, 7891 (2011).
[25] J. Eloranta and V. A. Apkarian, J. Chem. Phys. **117**, 10139 (2002).
[26] J. Eloranta, N. Schwentner, and V. A. Apkarian, J. Chem. Phys. **116**, 4039 (2002).
[27] D. Mateo, D. Jin, M. Barranco, and M. Pi, J. Chem. Phys. **134**, 044507 (2011).
[28] H. J. Maris, J. Low Temp. Phys. **120**, 173 (2000).
[29] M. Rosenblit and J. Jortner, Phys. Rev. Lett. **75**, 4079 (1995).
[30] A. P. Hickman, W. Steets, and N. F. Lane, Phys. Rev. B **12**, 3705 (1975).
[31] J. Jortner, W. R. Kestner, S. A. Rice, and M. H. Cohen, J. Chem. Phys. **43**, 2614 (1965).
[32] K. Hirioke, N. R. Kestner, S. A. Rice, and J. Jortner, J. Chem. Phys. **43**, 2625 (1965).
[33] A. P. Hickman and N. F. Lane, Phys. Rev. Lett. **26**, 1216 (1971).
[34] R. C. Tolman, J. Chem. Phys. **17**, 333 (1949).
[35] J. Eloranta, Chem. Phys. **332**, 304 (2007).
[36] E. Krotscheck and J. Navarro, *Microscopic Approaches to Quantum Liquids in Confined Geometries* (World Scientific, New Jersey, 2002).
[37] J. Eloranta, H. Y. Seferyan, and V. A. Apkarian, Chem. Phys. Lett. **396**, 155 (2004).
[38] M. Barranco, R. Guardiola, S. Hernández, J. Navarro, and M. Pi, J. Low Temp. Phys. **142**, 1 (2006).
[39] A. Hernando, M. Barranco, R. Mayol, M. Pi, F. Ancilotto, O. Bünermann, and F. Stienkemeier, J. Low Temp. Phys. **158**, 105 (2010).
[40] D. Mateo, M. Barranco, R. Mayol, and M. Pi, Eur. Phys. J. D **52**, 63 (2009).
[41] F. Dalfovo, A. Lastri, L. Pricaupenko, S. Stringari, and J. Treiner, Phys. Rev. B **52**, 1193 (1995).
[42] F. Ancilotto, F. Faccin, and F. Toigo, Phys. Rev. B **62**, 17035 (2000).
[43] M. Hartmann, F. Mielke, J. P. Toennies, A. F. Vilesov, and G. Benedek, Phys. Rev. Lett. **76**, 4560 (1996).
[44] P. W. Anderson, Phys. Rev. **86**, 809 (1952).
[45] H.-J. Werner *et al.*, MOLPRO *Version 2010.1, A Package of ab initio Programs* (2010), see [http://www.molpro.net].
[46] P. J. Knowles and N. C. Handy, Comput. Phys. Commun. **54**, 75 (1989).
[47] F. Boys and F. Bernardi, Mol. Phys. **19**, 553 (1970).

[48] T. Kiljunen, J. Eloranta, and H. Kunttu, J. Chem. Phys. **110**, 11814 (1999).
[49] J. Ahokas, T. Kiljunen, J. Eloranta, and H. Kunttu, J. Chem. Phys. **112**, 2420 (2000).
[50] K. K. Sunil, J. Lin, H. Siddiqui, P. E. Siska, K. D. Jordan, and R. Shepard, J. Chem. Phys. **78**, 6190 (1983).
[51] C. F. Chabalowski, J. O. Jensen, D. R. Yarkony, and B. H. Lengsfield, J. Chem. Phys. **90**, 2504 (1989).
[52] B. Deguilhem, Ph.D. thesis, Université de Toulouse, 2009, (unpublished).
[53] V. D. Arp, R. D. McCarty, and D. G. Friend, *NIST Technical Note 1334 (revised): Thermophysical Properties of Helium-4 from 0.8 to 1500 K with Pressures to 2000 MPa* (National Institute of Standards and Technology, Boulder,1998).
[54] L. Lehtovaara, J. Toivanen, and J. Eloranta, J. Comp. Phys. **221**, 148 (2007).
[55] L. Lehtovaara, T. Kiljunen, and J. Eloranta, J. Comp. Phys. **194**, 78 (2004).
[56] L. Lehtovaara and J. Eloranta, *3-D Implementation of the Orsay-Trento Helium Density Functional* [http://libdft.sourceforge.net].
[57] L. Lehtovaara and J. Eloranta, *Parallel Library for Processing Cartesian Grids* [http://libgrid.sourceforge.net].
[58] J. Wilks, *The Properties of Liquid and Solid Helium* (Clarendon Press, Oxford, 1967).
[59] J. C. Hill, O. Heybey, and G. K. Walters, Phys. Rev. Lett. **26**, 1213 (1971).
[60] G. Herzberg, *Molecular Spectra and Molecular Structure: I. Spectra of Diatomic Molecules*, 2nd ed. (Van Nostrand, Princeton, 1950).
[61] N. F. Allard, N. Bonifaci, and A. Denat, Eur. Phys. J. D **61**, 365 (2011).
[62] S. L. Fiedler, E. A. Popov, and J. Eloranta (unpublished).
[63] G. W. F. Drake, *Atomic, Molecular & Optical Physics Handbook* (AIP, Woodbury, 1996).